chemengineering

MDPI

Article

Oxalic Acid-Assisted Photo-Fenton Catalysis Using Magnetic Fe_3O_4 Nanoparticles for Complete Removal of Textile Dye

Sunil Bhavsar [1], Pravin Dudhagara [1,*], Anjana Ghelani [2], I Nengah Wirajana [3], Quyet-Tien Phi [4], Yih-Yuan Chen [5] and Douglas J. H. Shyu [6,*]

1 Department of Biosciences, Veer Narmad South Gujarat University, Surat 395007, Gujarat, India; spbhavsar@vnsgu.ac.in
2 Shree Ramkrishna Institute of Computer Education and Applied Sciences, Sarvajanik University, Surat 395001, Gujarat, India; anjana.ghelani@srki.ac.in
3 Department of Chemistry, Faculty of Mathematics and Natural Science, Udayana University, Badung 80361, Indonesia; nengah_wirajana@unud.ac.id
4 Institute of Biotechnology, Vietnam Academy of Science and Technology, Hanoi 100000, Vietnam; tienpq@ibt.ac.vn
5 Department of Biochemical Science and Technology, National Chiayi University, Chiayi City 600, Taiwan; yychen@mail.ncyu.edu.tw
6 Department of Biological Science and Technology, National Pingtung University of Science and Technology, Pingtung 912301, Taiwan
* Correspondence: pravindudhagara@vnsgu.ac.in (P.D.); dshyu@mail.npust.edu.tw (D.J.H.S.); Tel.: +91-9428204093 (P.D.); +886-8-7703202 (ext. 6367) (D.J.H.S.)

Abstract: Textile industry effluents contain several hazardous substances, such as dye-containing effluents, which pose environmental and aesthetic challenges. Presently, the microbial-based remediation process is in use. This study investigated the application of ferrous–ferric oxide (Fe_3O_4) nanoparticles, a readily formulated nanoadsorbent, to remove scattered dye molecules from industrial effluents. The ferrous–ferric oxide nanoparticles were prepared using a chemical co-precipitation method. The nanoparticles had 26.93 emu g^{-1} magnetization, with sizes smaller than 20 nm, and possessed a highly purified cubic spinel crystallite structure. The catalytic activity of the iron oxide depended on the dose, photocatalytic enhancer, i.e., H_2O_2 level, pH of the reaction medium, and dye concentration. We optimized the Fenton-like reaction to work best using 1.0 g/L of ferrous–ferric oxide nanoparticles, 60 mM oxalic acid at pH 7.0, and 60 ppm of dye. Iron oxides act as photocatalysts, and oxalic acid generates electron–hole pairs. Consequently, higher amounts of super-radicals cause the rapid degradation of dye and pseudo-first-order reactions. Liquid chromatography–mass spectrometry (LC-MS) analysis revealed the ferrous–ferric oxide nanoparticles decolorized and destroyed Disperse Red 277 in 180 min under visible light. Hence, complete demineralization is observed using a photo-Fenton-like reaction within 3 h under visible light. These high-capacity, easy-to-separate next-generation adsorption systems are suggested to be suitable for industrial-scale use. Ferrous–ferric oxide nanoparticles with increased adsorption and magnetic properties could be utilized to clean environmental pollution.

Keywords: magnetic iron oxide nanoparticles; photocatalysts; dye degradation; Fenton-like reaction; Fe_3O_4 nanoparticles

Citation: Bhavsar, S.; Dudhagara, P.; Ghelani, A.; Wirajana, I.N.; Phi, Q.-T.; Chen, Y.-Y.; Shyu, D.J.H. Oxalic Acid-Assisted Photo-Fenton Catalysis Using Magnetic Fe_3O_4 Nanoparticles for Complete Removal of Textile Dye. *ChemEngineering* **2024**, *8*, 67. https://doi.org/10.3390/chemengineering8040067

Academic Editors: Chrysoula Athanasekou and Nikolaos G. Moustakas

Received: 15 May 2024
Revised: 19 June 2024
Accepted: 26 June 2024
Published: 28 June 2024

1. Introduction

The textile industry in India is one of the country's oldest, dating back several centuries. The fundamental strength of India's textile industry is its large production base of natural and synthetic fibers and yarns. The current demand for colorful clothes necessitates the use of a large number of synthetic dyes to enhance the aesthetic value of the textile. Azo dyes account for approximately 70% of all dyes, making them the most widely used type of dye on a global scale due to their stability, color variety, and low cost of synthesis.

Textiles use over 3000 types of azo dyes to create various colors [1]. As a result, the textile industries produce a large amount of colored effluent. Textile industry effluents, laden with toxic metals and high in COD are unfit for environmental discharge [2]. Excessive dye-laden wastewater negatively impacts the growth of aquatic plants and algae by reducing their photosynthetic activity. Azo dyes are widely used in the textile printing and paper industries due to their ability to directly stain fibers without a mordant (fixative) but pose a significant environmental concern [3]. Furthermore, because of their vibrant colors, affordable price, and resistance to bleaching and repeated washing, azo dyes are widely used in the textile industry to color cellulosic fibers such as cotton and wool. The majority of azo dyes have the potential to be toxic, carcinogenic, mutagenic, or allergenic. Most textile industries in India lack specialized facilities for treating dye-laden wastewater. As a result, such industrial units transport waste to centralized and shared treatment plants managed by government agencies. Various methods are used to treat industrial wastewater, including chemisorption and physisorption, membrane filtration, ion exchange, chemical oxidation, and biological treatment [4]. Finally, effluent treatment raises costs due to transportation or multiple treatment technologies.

Disperse azo dyes are polar molecules containing anthraquinone or azo groups. Due to their non-ionic properties in nature and being partially soluble in water, dispersed dyes are not easily removed from the conventional treatment process [5,6]. Chemical oxidation or biological treatment typically decolorizes dyes, but these methods may not reduce their toxicity. The traditional approaches for removing dyes are not viable since they are costly, cumbersome, non-destructive, and ultimately ineffective because they convert pollutants into sludge, giving rise to new pollution that necessitates additional clean technologies.

There is a rising demand for a low-cost, sustainable technique of pollutant removal as chemicals from pharmaceutical and agricultural products, as well as hazardous waste from industrial sources that do not naturally decay, end up in the environment. Photocatalysis is an environmentally beneficial technique that is capable of targeting multiple types of pollutants [7]. The photochemical breakdown of harmful compounds into simple and non-toxic species owing to exposure to light is an advanced oxidation process (AOP) currently used for pollution cleanup. Photocatalysis with nanoparticles shows great promise for treating industrial effluent because of its low-cost, environmentally friendly method, effective antibacterial capability [8], lack of secondary contamination, and non-selective degrading of diverse organic dyes into CO_2 and H_2O. Fe_3O_4 is a viable choice for photocatalytic applications due to its lack of secondary pollution, n-type semiconducting behavior, and 2.1 eV bandgap, which advanced visible light photocatalysis [9]. When visible light strikes Fe_3O_4, photons with sufficient energy can excite an electron from the valence band (VB) to the conduction band (CB), generating an electron–hole pair (exciton). The exciton acts as the initial spark in photocatalysis. Its separation into energetic electron and hole carriers drives the redox reactions that drive the photocatalytic magic [10]. AOP can degrade organic pollutants without discrimination because the free radicals produced by adding strong oxidants speed up the degradation process. For powerful oxidants and adsorbents, however, these approaches can cause secondary pollution issues [11]. Superoxide and hydroxyl radicals generated by photosensitization can non-selectively destroy the structure of the most recalcitrant organic pollutants in wastewater [12,13], making the photocatalytic oxidation technique a green way to degrade organic pollutants. The photocatalytic method requires only photocatalysts and does not pollute the environment [14]. Graphene, metal semiconductors, and precious metals seem to be the mainstays of photocatalysts [15,16]. However, there has been limited exploration of Fe_3O_4 nanoparticles. Fe_3O_4 with oxalic acid forms ferrioxalate photoactive complexes. They are highly photocatalytic and cause the photodegradation of dye. Therefore, we need an eco-friendly photocatalyst for effluent remediation, such as a solid-phase Fe_3O_4 nanoparticle, which can be separated from heterogeneous systems using magnetic separation [17]. As a result of these benefits and suitability, Fe_3O_4 nanoparticles would be a good candidate for removing textile dye in an aqueous liquid medium.

Fe_3O_4 nanoparticles have emerged as excellent nanomaterials for developing functional materials with various surface functions such as degradation, adsorption, and simple separation due to magnetism, and they have already demonstrated promising results in bioremediation processes. Fe_3O_4 nanoparticles can remove color and break down BR 46 azo dye well in ideal conditions and at high dye concentrations [18]. Furthermore, magnetic nanoparticles can easily be combined with other metals to form spinel ferrite nanoparticles, less expensive magnetic materials that remain stable under various conditions [19]. Magnetic mesocrystals of iron oxide formed by bacteria are helpful for industrial effluent treatment and have the potential for bioremediation. The recovery and recycling of magnetic nanoparticles in wastewater treatment are features of these nanoparticles that make them suitable for industrial applications [20].

The current study used a simple, one-step method to prepare a magnetic Fe_3O_4 photocatalyst. SEM, TEM, XRD, UV-Vis, and VSM were used to characterize the photocatalysts. A photo-Fenton-like reaction is optimized using several variables to achieve the maximum Disperse Red 277 degradation. The research contributes to applying nanoscale Fe_3O_4 as a promising future application in the photodegradation of azo dyes in wastewater remediation.

2. Materials and Methods

2.1. Chemicals

$FeCl_3$ (Ferric chloride), $FeSO_4$ (Ferrous sulfate), HCl (Hydrochloric acid), H_2SO_4 (Sulfuric acid), NH_4OH (Ammonium hydroxide), H_2O_2 (Hydrogen peroxide) 30% v/v, and $C_2H_2O_4$ (Oxalic acid) were used in the experiment. All the chemicals were of A. R. grade and purchased from HiMedia Laboratories Private Limited, Mumbai, India. Disperse Red 277 ($C_{24}H_{23}N_5O$) (CAS No. 70294-19-8, Molecular weight 397.47) (Figure 1) was purchased from the regional textile manufacturing market of Surat, Gujarat, India.

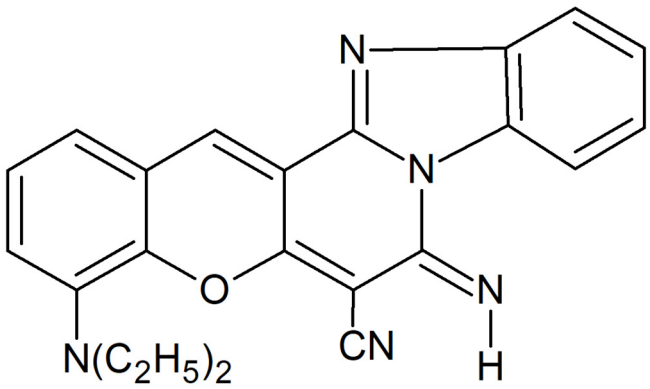

Figure 1. The chemical structure of Disperse Red 277 ($C_{24}H_{23}N_5O$).

2.2. Synthesis of Magnetic Ferrous–Ferric Oxide Nanoparticles

Co-precipitation was used to create metal oxide nanoparticles [21,22]. In a typical synthesis, the co-precipitation of various metal salts (nitrates, sulfates, or chlorides) using aqueous NH_3, NaOH or $NaHCO_3$ solutions results in the precipitation of the corresponding metal hydroxide. The precipitate was washed twice with double-distilled water to remove $SO_4{}^{-2}$, $NO_3{}^{-}$, and Cl^{-} ions. Co-precipitation often results in nanoparticles with increased interoperability and chemical homogeneity.

For the co-precipitation method of production of magnetic nanoparticles, 3.7 g of $FeCl_3$ (Ferric chloride) and 9.54 g of $FeSO_4$ (Ferrous sulfate) were combined separately in 500 mL of sterile deionized water. Later, both were added to a 1000 mL Erlenmeyer's flask and swirled for 10 min at 80 °C. After mixing, 20 mL of NH_3 solution was added to see the color change from orange to black [21–23].

2.3. Characterization Study

Various techniques were used to characterize formulated nanoparticles. Using Cu-K irradiation in an X-ray diffractometer, powder XRD patterns were determined (Xpert MPD, Philips, Almelo, The Netherlands) with the Joint Committee on Powder Diffraction Standards (JCPDS) (JCPDS Card No. 019-0629) [24] powder diffraction structural designations. The functional group of nanopowder was determined using Fourier transform infrared spectroscopy (FTIR, SPECTRUM GX, Perkin Elmer, Waltham, MA, USA). In secondary and backscattered electron modes, surface morphology was studied using scanning electron microscopy (SEM, Nova Nano FEG-SEM 450, FEI, Hillsboro, OR, USA). Energy-dispersive X-ray analysis (EDX) (TEAM EDS, FEI, Hillsboro, OR, USA) connected to the SEM was used for elemental analysis. The surface morphology and size were also examined using transmission electron microscopy (TEM, TECNAI 20, Philips, Almelo, The Netherlands). The particle magnetism was analyzed using a vibrating-sample magnetometer (VSM). Particle and dye spectra were determined using UV–visible spectroscopy.

2.4. Photo-Fenton Reaction for Photosensitized Dye Degradation

The decolorization of the Disperse Red 277 dye in an aqueous solution was assessed to determine the photocatalytic activity. The studies were conducted in visible light (light intensity approx. 2500–3000 Lumens) with ferrous–ferric oxide nanoparticles in the photocatalytic reactor. The reaction was initiated by dissolving 0.1 g of the synthesized powder in 100 mL of dye solution (50 mg/L) in a beaker, then magnetically stirring the suspension for 30 min in the dark with 60 mM H_2O_2. This 30 min time is to saturate the reaction and will consider the start of the reaction, i.e., zero minutes. Afterwards, the solution was kept at room temperature during the process, and the lamp was placed 9 cm away from the solution to illuminate the beaker after achieving the adsorption/desorption equilibrium.

Ten milliliters of the solution were taken every 30 min after illumination for 180 min. Before measuring absorbance, the suspension was centrifuged at 5000 rpm for 10 min, and a filter was used to remove the catalyst particles of the supernatant. For quantitative analysis, the absorbance of the supernatant was determined at a wavelength of 570 nm. Visible light was generated using an incandescent bulb with a specific power of 220 V, 27 W, and 50 Hz. The following Equation (1) was used to calculate the percentage degradation of Disperse Red 277 dye.

$$\text{Degradation } (\%) = \frac{(A_0 - A_t)}{A_0} \times 100 \quad (1)$$

where A_0 is the absorbance (570 nm) of Disperse Red 277 measured at the beginning, and A_t is the absorbance of Disperse Red 277 measured at time t.

2.4.1. Optimized Conditions for Dye Degradation

Several parameters affect the degradation of Disperse Red 277, including dye concentration, oxidizing agent H_2O_2 concentration, ferrous–ferric oxide nanoparticles, and pH. Each parameter was evaluated to find the optimized conditions for Disperse Red 277 degradation and the percentage degradation as measured in Equation (1).

2.4.2. Mimicry of Photo-Fenton Reaction Using Oxalic Acid

Being an oxidizing agent, 60 mM oxalic acid was used in the photo-Fenton reaction above to replace the H_2O_2 in dye degradation in the presence of light. This mimicry-reaction-mediated dye degradation was then subjected to chromatographic analysis to check the dye removal. Control reactions were also performed without the nanoparticles using 60 mM oxalic acid, 60 mM H_2O_2, and 50 ppm dye.

2.5. Liquid Chromatography–Mass Spectrometry (LC-MS)

LC-MS is advantageous for the fast detection and structural identification of compounds. A solvent gradient was set up as an initial water and acetonitrile ratio of 40:60, and then the amount of acetonitrile was linearly raised to 100% within 16 min. The acetonitrile concentration was maintained at 100% for 9 min to clean the C18 column; the re-equilibration time was 5 min. The flow rate of the mobile phase was 1 mL min^{-1}, and the volume for the injection was 40 mL. Direct injection was used for each component to optimize MS parameters, such as the declustering potential and the collision energy. The following were the optimized ion source parameters: curtain gas pressure (CUR) at 18 psi, ion spray voltage (IS) at 5000 V, nebulizer gas pressure (GAS1) at 40 psi, turbo heater gas pressure (GAS2) at 50 psi, and temperature at 500 °C. High pressure was applied to the gas for collision-activated dissociation (CAD).

3. Results

3.1. Synthesis of Magnetic Ferrous–Ferric Oxide Nanoparticles

Magnetic ferrous–ferric oxide nanoparticles were prepared using a chemical co-precipitation method [22]. These nanoparticles are also known as iron oxide black nanoparticles due to their characteristic black color. The maximum absorption peak at 333.50 nm in the UV-visible spectrum indicated the synthesis of magnetic ferrous–ferric oxide nanoparticles in water (Figure 2). The narrow, bell-shaped appearance of the graph suggests the very controlled synthesis of the nanoparticles.

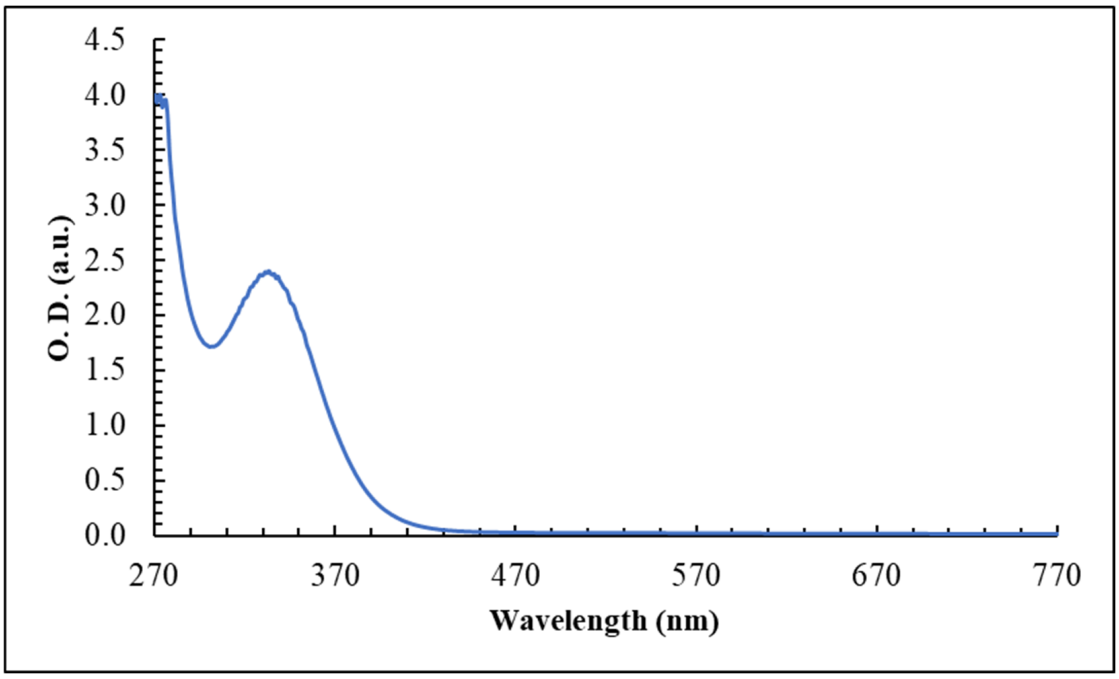

Figure 2. The UV-visible spectrum of synthesized magnetic ferrous–ferric oxide nanoparticles. A sharp, heightened, and narrow peak at 333.50 nm indicates the Fe_3O_4 nanoparticle formulation.

3.2. Characterization of Ferrous–Ferric Oxide Nanoparticles

3.2.1. XRD

The X-ray diffraction patterns of the synthesized magnetic ferrous–ferric oxide nanoparticles were analyzed to confirm the composited component's impact on the overall crystal structure (Figure 3). The heating temperature for samples was 250 °C. The prepared ferrous–ferric oxide nanoparticles revealed diffraction peaks at 2θ = 30.11°, 35.66°, 43.38°, 53.84°, 57.28°, 62.64°, 71.43°, and 74.52° from crystalline planes indexed to (220), (311), (400), (422), (511), (440), (620) and (533), miller indices, respectively (Table 1), which are represented to

the crystalline phase of magnetite. The (210) and (211) peaks were not seen in the diffraction pattern which is more obvious in maghemite [25]. The peaks are the characteristics of a ferrous–ferric oxide crystal with a cubic spinel structure, consistent with the database's JCPDS file No. 19-0629 [24,26]. The particle size is small, and the average diameter is 20.66 nm, estimated from Scherrer's equation.

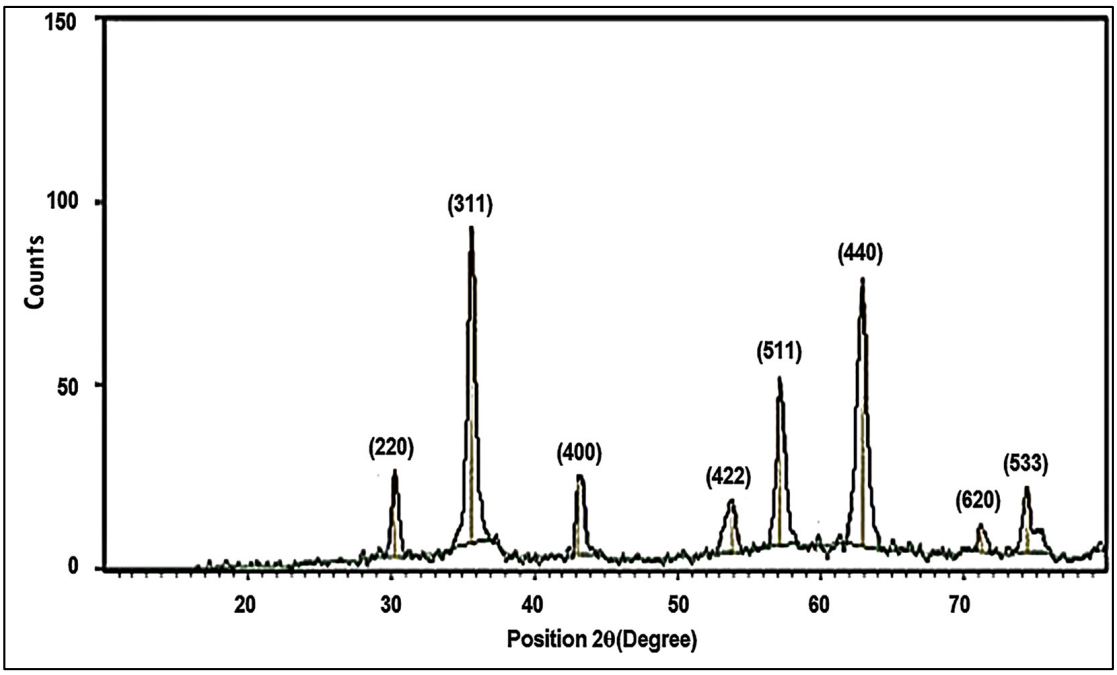

Figure 3. XRD patterns of ferrous–ferric oxide nanoparticles.

Table 1. XRD data of synthesized ferrous–ferric oxide nanoparticles.

Position [°2θ]	FWHM * [°2θ]	*d*-Spacing [Å]	Height [cps]	Relative Intensities [%]	Significance	Miller Indices *hkl*	Structure	Particle Size (nm)
30.11	0.4428	2.95412	23.78	27.02	2.4779	220		19.41
35.66	0.4920	2.52352	88.01	100.00	5.9428	311		17.72
43.38	0.4428	2.10187	20.00	22.73	2.3232	400		20.18
53.84	0.6888	1.70288	13.86	15.75	2.0597	422	Cubic	13.52
57.28	0.3936	1.61336	42.46	48.25	2.1600	511	spinel	24.08
62.64	0.3444	1.47759	71.86	81.66	1.3618	440		28.22
71.43	0.5904	1.32271	6.60	7.50	1.3419	620		17.32
74.52	0.4200	1.27388	17.73	20.15	1.0193	533		24.84

* FWHM: full width at half maximum.

The highly intense dominating reflection peaks of the XRD pattern used in the line broadened the analysis of the samples. The Williamson–Hall plot fitted near a straight line supporting the crystallite size and lattice strain measured by XRD (Figure 4). Here, the X-axis represents a function combining the diffraction angle (theta) and the sine of theta, and the Y-axis represents a function combining the full width at half maximum (FWHM) of the diffraction peak, corrected for instrumental broadening, and the cosine of theta.

3.2.2. FTIR

The FTIR spectrum of ferrous–ferric oxide nanoparticles showed peaks near 597 cm^{-1}, which was related to the existence of magnetic component (Fe–O) stretch vibrations (Figure 5) [27,28]. It also denotes the purity of the magnetite particle.

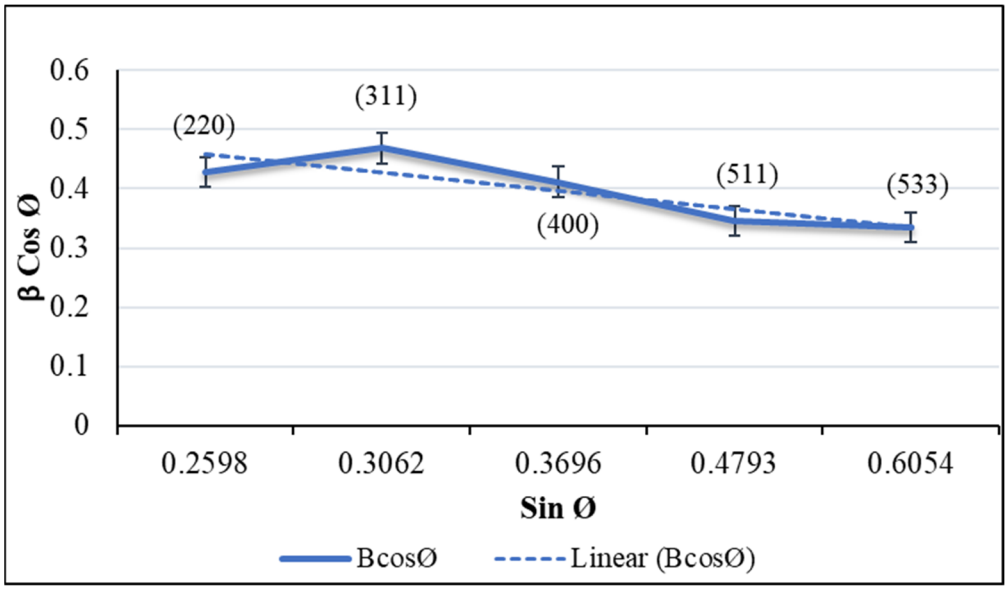

Figure 4. The Williamson–Hall plot (βcosθ vs. sinθ) of ferrous–ferric oxide nanoparticles obtained from XRD.

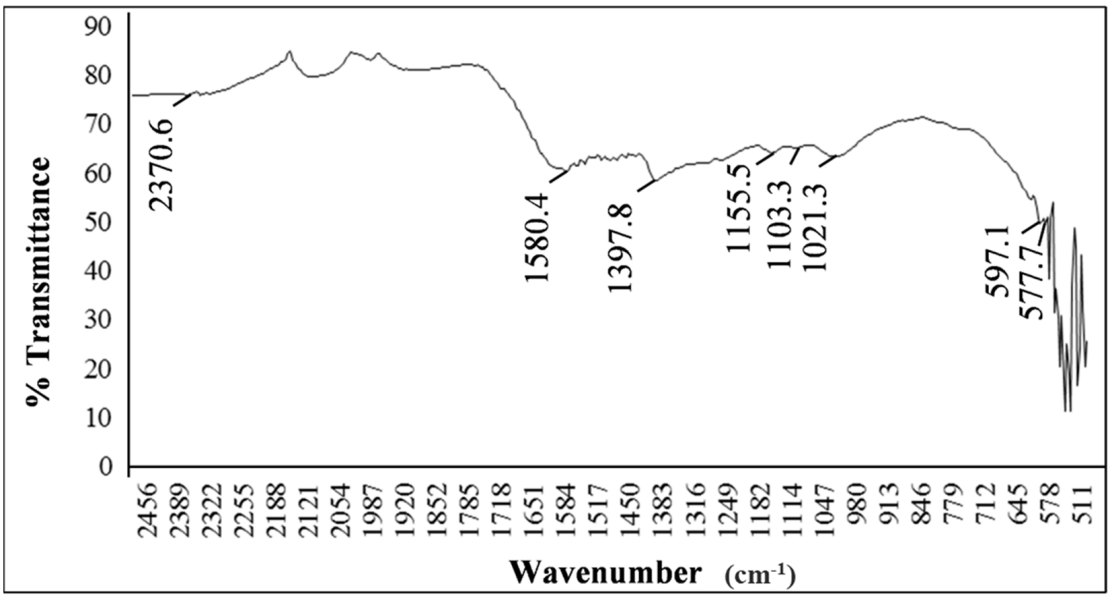

Figure 5. FTIR spectrum of ferrous–ferric oxide nanoparticles. Peaks at 597.1 cm^{-1} indicate (Fe–O) stretch vibrations of nanoparticles.

3.2.3. SEM and EDX

Because of the high dipole–dipole interactions among the uncapped nanoparticles (Figure 6A) and the inherent agglomeration and minimum dimension of ferrous–ferric oxide nanoparticles, it seemed challenging to estimate the particle size from scanning electron microscopy (SEM) images. EDX was used for the elemental analysis of ferrous–ferric oxide nanoparticles. The spectrum showed two significant peaks in which elements Fe and O had a maximum atomic percentage of 22.25% and 45.11%, respectively. The presence of a small peak of sulfur was obvious due to the use of ferrous sulfates in the synthesis process of the nanoparticles. During the synthesis, unreacted sulfate ions, or partially formed iron sulfide, were detected as impurities within the final product (Table 2). The characteristic peaks of Fe and O suggested the presence of high-purity ferrous–ferric oxide nanoparticles. (Figure 6B).

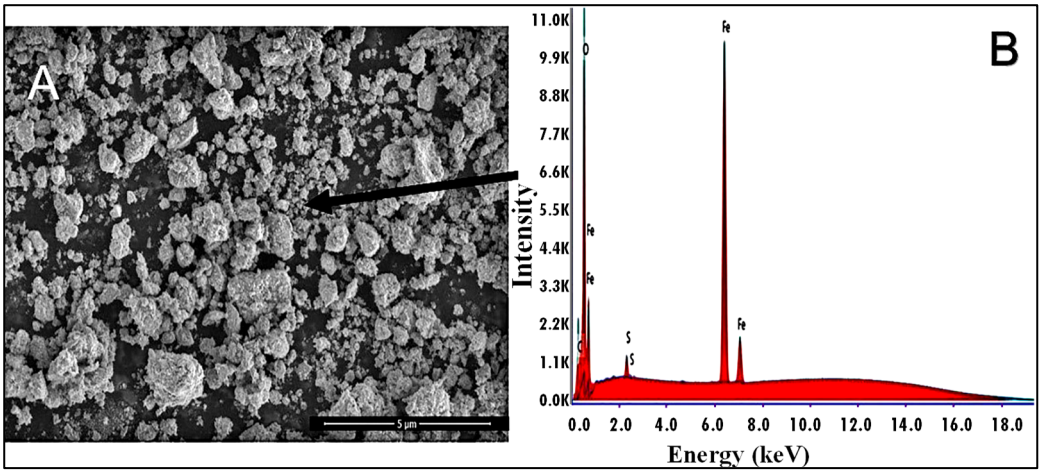

Figure 6. (**A**) SEM image of ferrous–ferric oxide nanoparticles; (**B**) EDX spectrum for ferrous–ferric oxide nanoparticles. The arrow in (**A**) indicated the small and delicate agglomeration of the ferrous–ferric oxide nanoparticles.

Table 2. Raw data of EDX spectrum for ferrous–ferric oxide nanoparticles.

Element	Weight %	Atomic %	Net Intensities	Error %	K Ratio	Z	R	A
Fe	52.47	22.25	2910.82	1.77	0.46	0.86	1.05	1.01
O	30.48	45.11	1691.59	7.57	0.12	1.11	0.93	0.36
C	16.26	32.06	303.43	8.95	0.05	1.16	0.91	0.28
S	0.79	0.58	124.30	9.65	0.01	1.00	1.00	0.78

3.2.4. TEM

The TEM image showed the varied morphology of monodisperse ferrous–ferric oxide nanoparticles from irregular non-spherical to quasi-spherical shapes (Figure 7). They appeared as black, loose, and monodisperse nanoparticles.

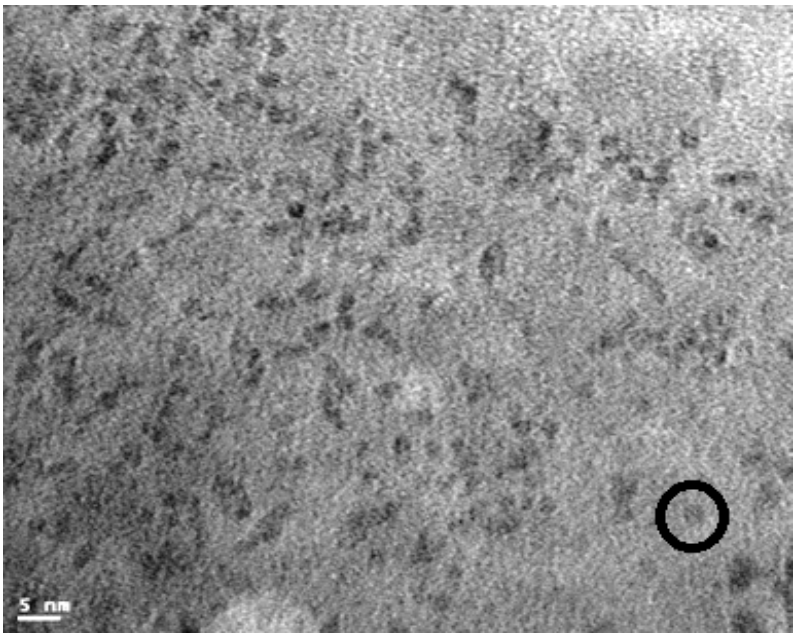

Figure 7. TEM image of ferrous–ferric oxide nanoparticles. The circled one is a quasi-spherical shape (particles vary in size, ranging from approximately 2.0 to 12.0 nm).

3.2.5. Magnetization

The magnetization of the ferrous–ferric oxide nanoparticles was investigated using VSM and analyzed at room temperature. The mass magnetization curve of ferrous–ferric oxide nanoparticles under the applied magnetic field is shown in Figure 8. The saturation magnetization was 26.93 emu g^{-1} for ferrous–ferric oxide nanoparticles.

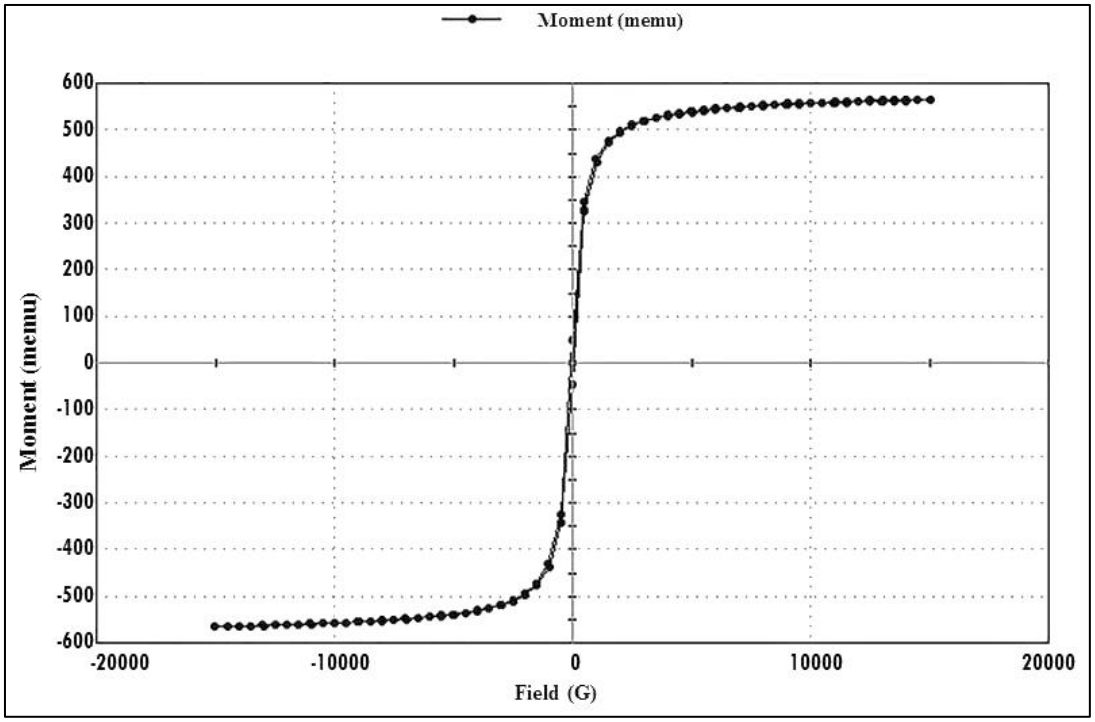

Figure 8. Vibrating sample magnetometer (VSM) measurements of ferrous–ferric oxide nanoparticles (mass: 0.021 g; magnetization: 0.56566 emu; number of points: 151; retentivity: 0.048862 emu; time constant: 1 s; sensitivity: −6.5000 emu).

3.3. Photocatalytic Dye Degradation

The photocatalytic dye degradation activity of ferrous–ferric oxide nanoparticles was evaluated using 50 ppm Disperse Red 277 under visible light (light intensity 2500–3000 Lumens). A UV-Vis spectral analysis was performed at the 400–700 nm range, and an absorption peak at 570 nm was observed. It was due to the excitation of surface plasmon vibrations in the ferrous–ferric oxide nanoparticles (Figure 9).

3.4. Optimized Conditions for Dye Degradation

Several parameters affect the degradation of Disperse Red 277, including dye concentration, oxidizing agent concentration, pH, and catalyst dose. Each parameter was evaluated to find the optimized degradation conditions for Disperse Red 277.

3.4.1. Effect of Dye Concentration

Ten different concentrations of dye solutions (10, 20, 30, 40, 50, 60, 70, 80, 90, and 100 ppm) were used at a fixed ferrous–ferric oxide nanoparticles (1.0 g/L) concentration. The results showed that the degradation rate decreased when a higher dye concentration was used (Figure 10). The degradation of Disperse Red 277 by ferrous–ferric oxide nanoparticles occurs by the adsorption of the dye onto the surface of the nanoparticles in the presence of a light source. The increased dye concentration would exceed the absorption capacity of ferrous–ferric oxide nanoparticles in a fixed concentration. The excess amount of dye molecules would not be adsorbed onto the surface of nanoparticles, leading to a decrease in the dye degradation percentage of higher dye concentration.

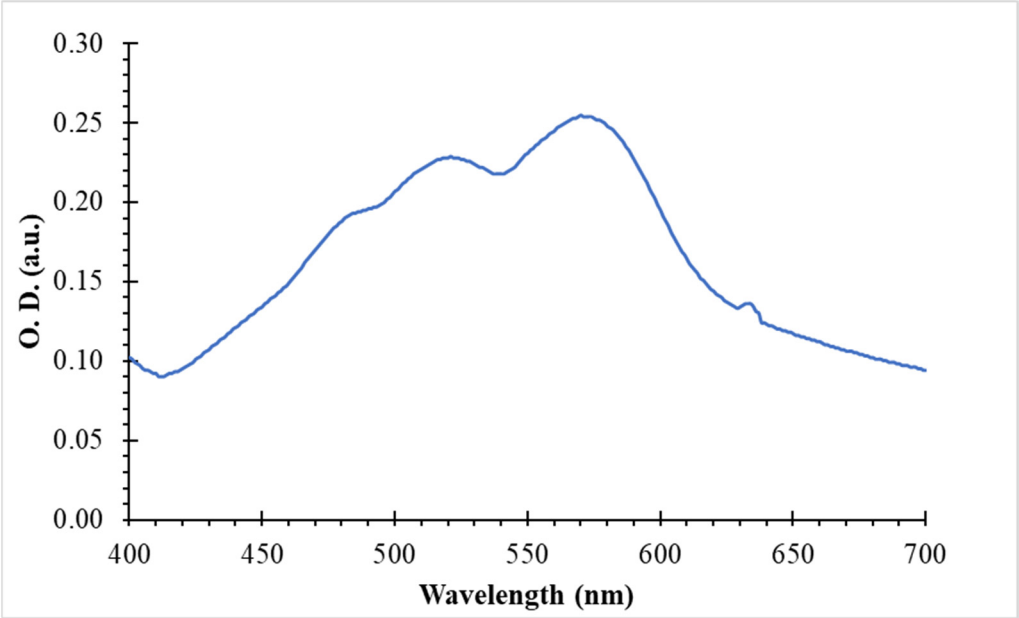

Figure 9. The UV-visible spectrum of photodegradation of 50 ppm Disperse Red 277 by ferrous–ferric oxide nanoparticles. The absorption peak is at 570 nm.

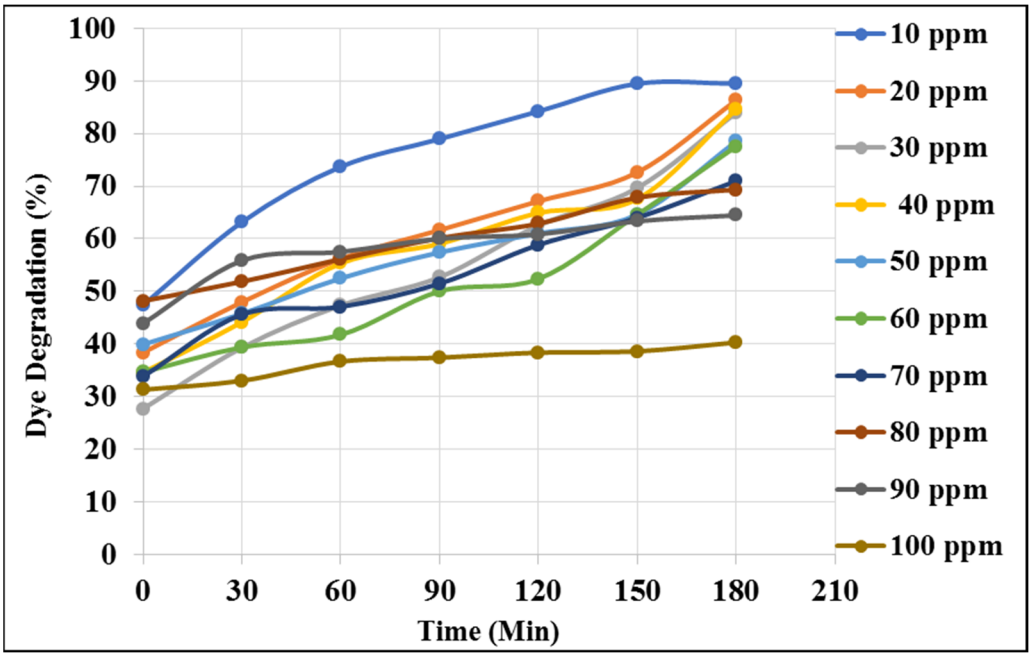

Figure 10. The degradation efficiency of Disperse Red 277 in different concentrations. The concentration of ferrous–ferric oxide nanoparticles was 1.0 g/L, and the reaction was performed at pH 7.0 (Zero-minute time is 30 min of incubation in the dark to saturate the reaction). A concentrated dye, i.e., 60, 70, 80, 90, and 100 ppm solution, was dissolved by heating at 80 °C temperature for 20 to 25 min.

3.4.2. Effect of H_2O_2 Concentration

A sequential 20 to 100 mM of H_2O_2 was added to provide a robust oxidizing condition to accelerate the dye degradation. The results showed that the dye degradation rate increased with an increased concentration of H_2O_2, especially in the initial 30 to 90 min (Figure 11). It indicated that a robust oxidizing condition was helpful in the Disperse Red 277 degradation efficiency of ferrous–ferric oxide nanoparticles. Ferrous–ferric ox-

ide nanoparticles would need longer to remove dye when a mild oxidizing condition is provided.

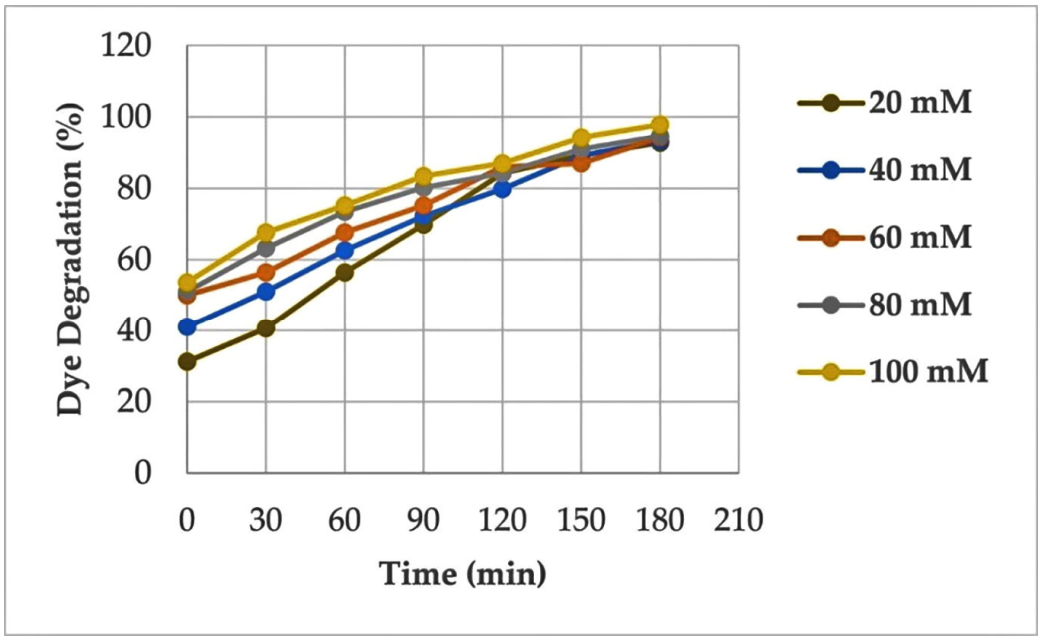

Figure 11. The degradation efficiency of Disperse Red 277 (60 ppm) with different concentrations of H_2O_2. The concentration of ferrous–ferric oxide nanoparticles was 1.0 g/L, and the reaction was performed at pH 7.0.

3.4.3. Effect of Ferrous–Ferric Oxide Nanoparticles Concentration

Since dye degradation occurs at the interface between ferrous–ferric oxide nanoparticles and water, the total area of the surface of the ferrous–ferric oxide nanoparticles would undoubtedly be one factor affecting the dye degradation rate. An increase in ferrous–ferric oxide nanoparticle concentrations would concurrently increase the surface area of ferrous–ferric oxide nanoparticles to react with dye molecules, leading to increased dye degradation. The results showed that dye degradation increased with an increase in ferrous–ferric oxide nanoparticles (Figure 12). However, 1.0 g/L was found to be best for dye degradation in 2 to 3 h.

3.4.4. Effect of pH

The pH of the solution changes the ionization state of the surface of ferrous–ferric oxide nanoparticles, which may affect the dye degradation efficiency. The results showed that the ferrous–ferric oxide nanoparticles exhibited higher dye degradation efficiency under neutral and acidic conditions (Figure 13). Moreover, it was suggested that the growth of the hydroxide layers on the surface of ferrous–ferric oxide nanoparticles could gradually reduce their interaction with Disperse Red 277 molecules, thereby decreasing dye degradation efficiency.

3.5. Photo-Fenton Reaction Mimicry Using Oxalic Acid

Oxalic acid can act as an oxidizing agent and is also helpful in dye degradation in the presence of light. To evaluate its effect on the dye degradation efficiency of ferrous–ferric oxide nanoparticles, 60 mM oxalic acid, compared with 60 mM H_2O_2, was used for the investigation (Figure 14). The results showed that oxalic acid increased dye degradation efficiency, like H_2O_2, shown in Figure 11. It indicated that an oxidizing condition generated by oxalic acid was as efficient as H_2O_2 for degrading Disperse Red 277 by a ferrous–ferric oxide nanoparticles-mediated Fenton-like reaction. Within 3 h, the complete removal of color was observed. Furthermore, the reaction was found to be a pseudo-first-order

reaction. The control reaction using 60 mM H_2O_2 indicated only 16.21% dye degradation within 3 h; whereas, using 60 mM oxalic acid indicated 20.27% degradation (Supplementary Tables S1 and S2).

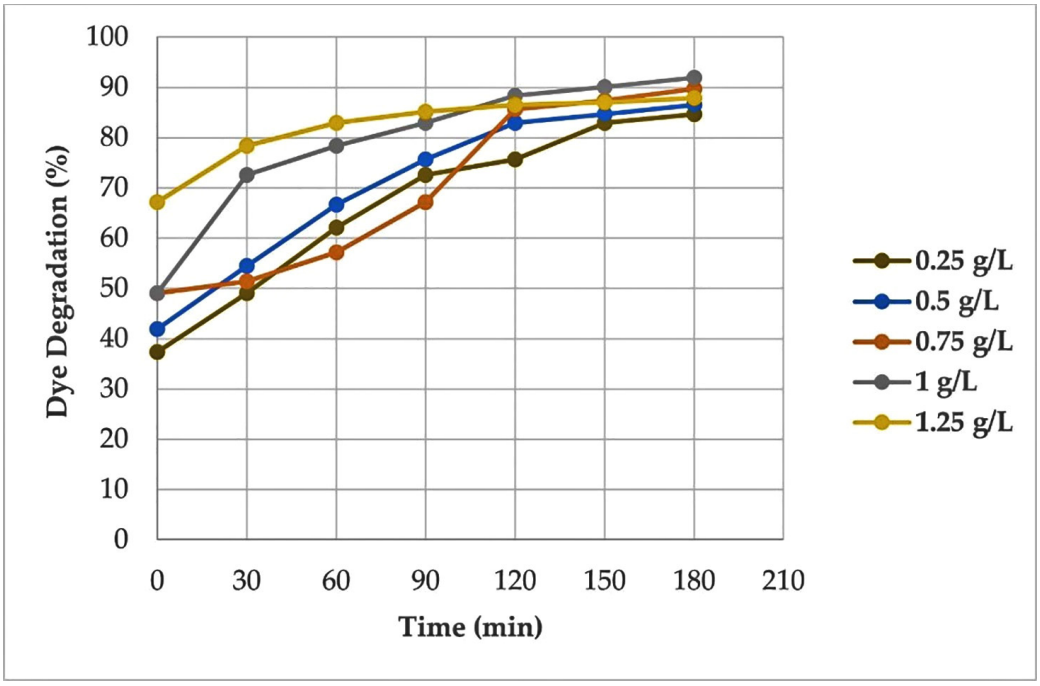

Figure 12. The degradation efficiency of Disperse Red 277 (60 ppm) with different concentrations of ferrous–ferric oxide nanoparticles (0.25 to 1.25 g/L). The concentration of H_2O_2 was 60 mM, and the reaction was performed at pH 7.0.

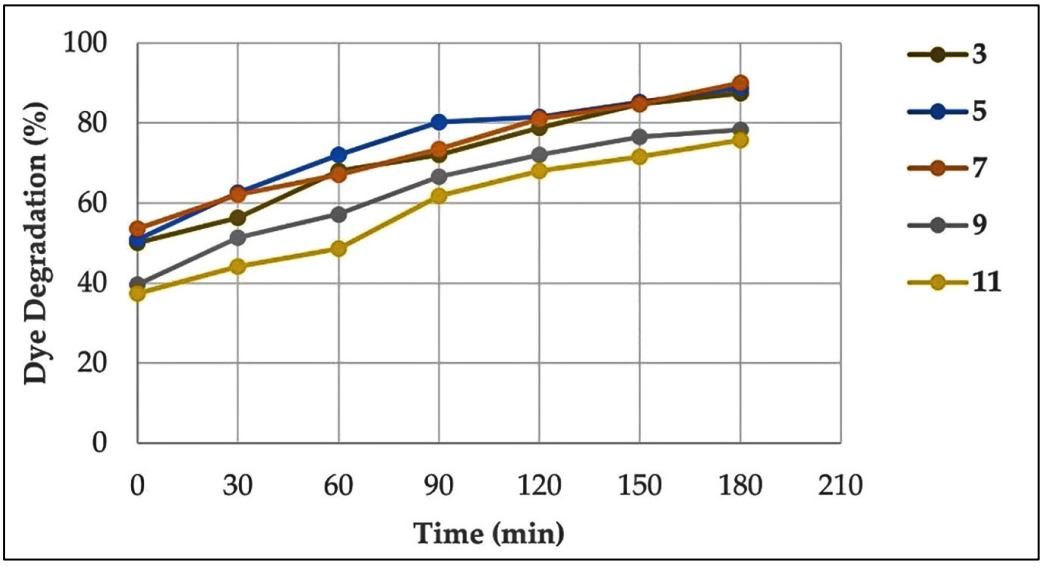

Figure 13. The degradation efficiency of Disperse Red 277 (60 ppm) under various pH conditions. The concentration of ferrous–ferric oxide nanoparticles was 1.0 g/L, and the concentration of H_2O_2 was 60 mM.

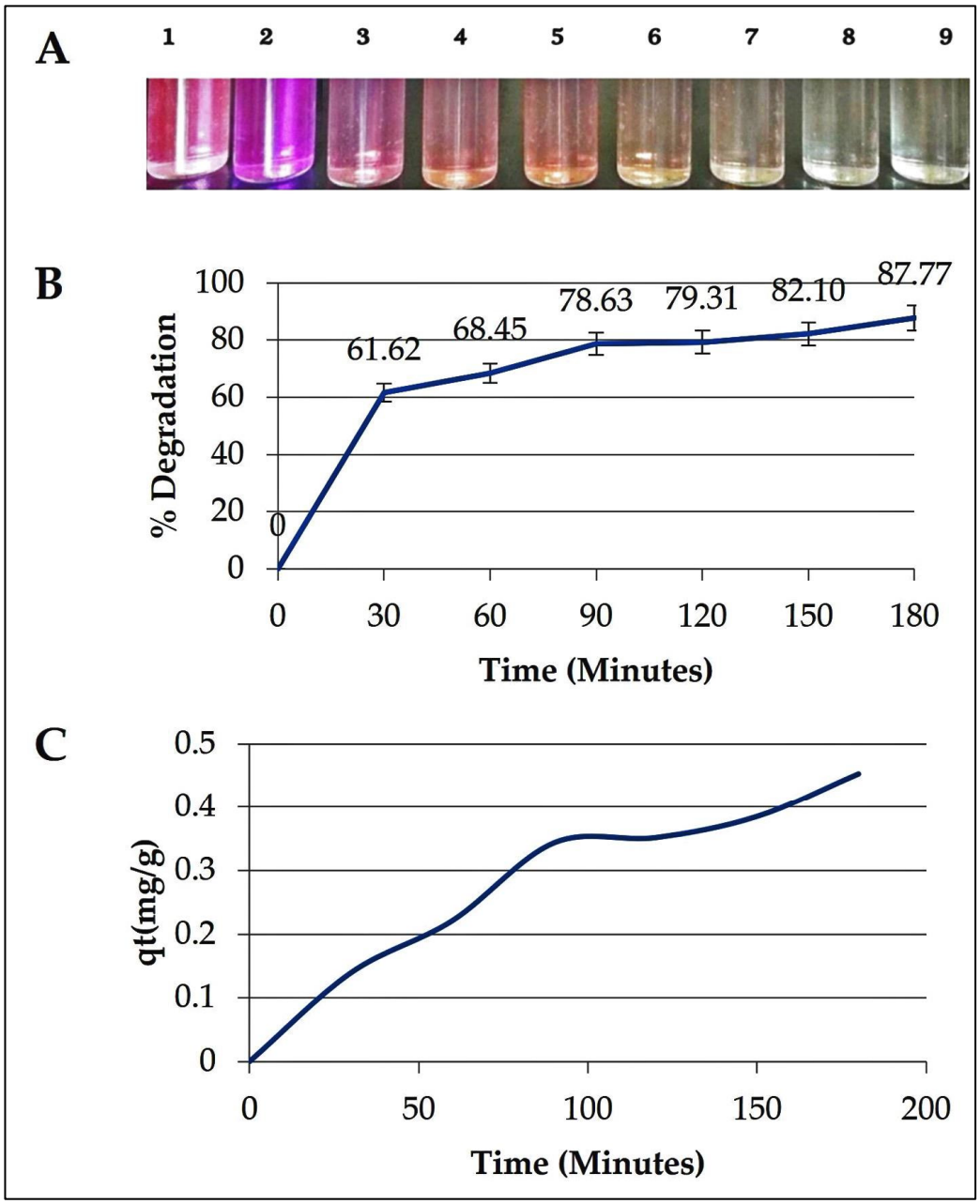

Figure 14. The degradation efficiency of Disperse Red 277 in the absence or presence of 60 mM oxalic acid. The concentration of ferrous–ferric oxide nanoparticles was 1.0 g/L, and the reaction was performed at pH 7.0. (**A**) 1: Control: dye only (60 ppm), 2: Fenton-like reaction containing dye (60 ppm), oxalic acid, and ferrous–ferric oxide nanoparticles, 3–9: 10, 30, 60, 90, 120, 150, and 180 min, respectively. (**B**) The degradation efficiency of Disperse Red 277 by the ferrous–ferric oxide nanoparticles in the presence of oxalic acid. (**C**) The amount of dye removed per unit mass of the synthesized sample (*qt*) was calculated using the (C_0–C_t) V/M equations, where C_0 and C_t are the concentration of dye at the initial stage, and after time *t*, V is the volume of the dye solution and M is the mass of the synthesized material.

3.6. LC-MS Analysis of Dye Degradation

LC-MS analysis was used to study the degradation of Disperse Red 277 by ferrous–ferric oxide nanoparticles. The results revealed that Disperse Red 277 was not degraded by ferrous–ferric oxide nanoparticles in the dark (Figure 15A), and the fraction was collected at a retention time of 23.66 min. It was confirmed by subjecting the fraction to present a

signal with an ion of a mass-to-charge (m/z) ratio of 383.25 detected by LC-MS analysis (Figure 15B). After exposure to the light, a Fenton-like reaction was mediated by ferrous–ferric oxide nanoparticles to degrade Disperse Red 277 in the light after 180 min (Figure 15C). The absence of a peak at the retention time of 23.66 min indicated the complete degradation of Disperse Red 277 by ferrous–ferric oxide nanoparticles.

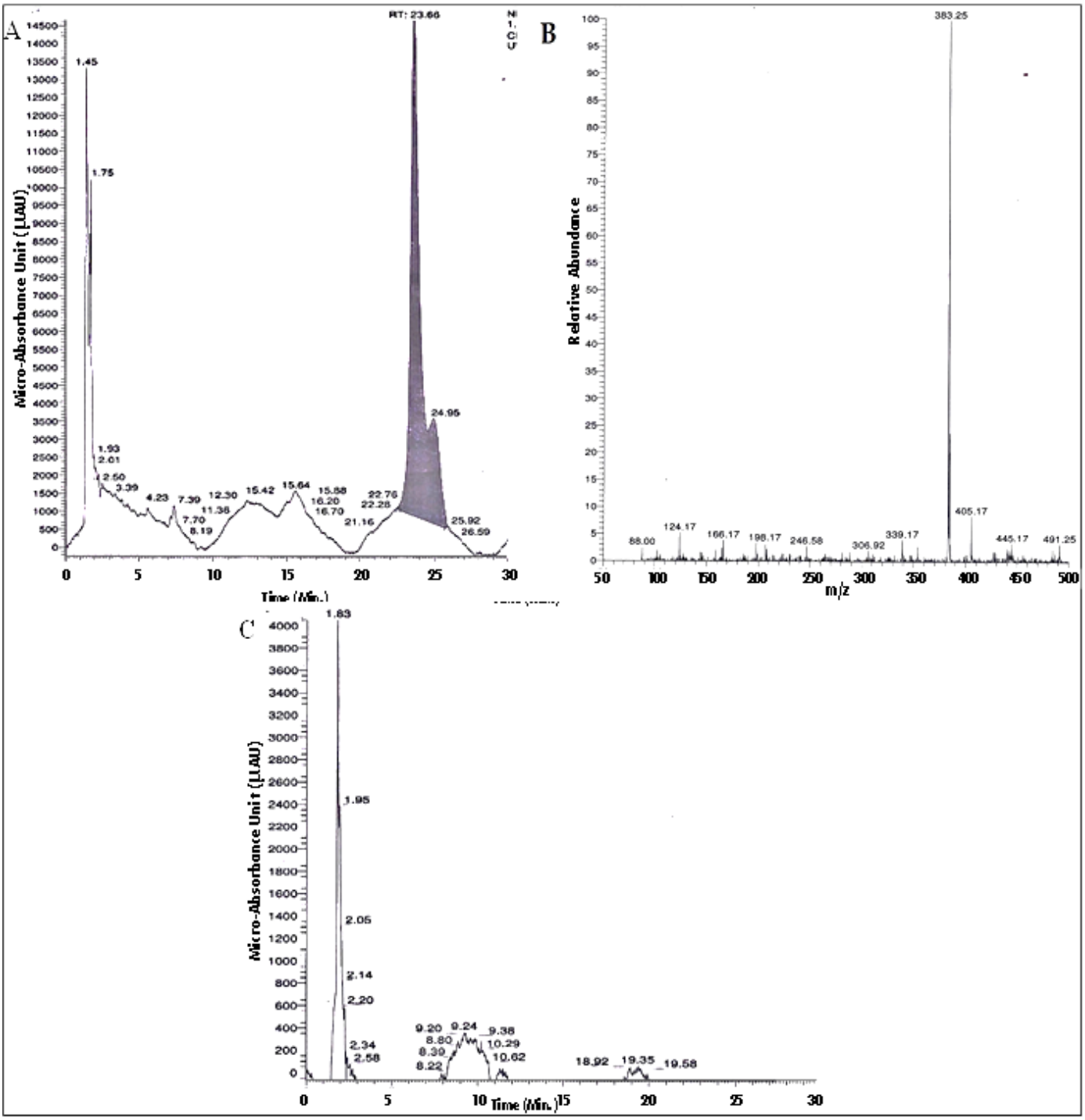

Figure 15. LC-MS analysis of (**A**) Disperse Red 277 before the Fenton-like reaction in the dark; (**B**) mass-to-charge (m/z) ratio analysis of Disperse Red 277 at retention time (RT) 23.66 min of (**A**); (**C**) Disperse Red 277 after the Fenton-like reaction under the light for 180 min. The concentration of ferrous–ferric oxide nanoparticles was 1.0 g/L, and the reaction was performed at pH 7.0 in the presence of 50 mg/L Disperse Red 277.

4. Discussion

The properties of adsorption, combined with magnetic separation, were effectively applied in the treatment of environmental wastewater and pollutants [28,29]. The saturation magnetization of synthesized ferrous–ferric oxide nanoparticles was determined to be 26.93 emu g^{-1}. It was adequate to separate them magnetically using a magnet [30]. In addition, organic pollutants, including dyes and other chemicals, were useful magnetic adsorbents to adsorb ferrous–ferric oxide nanoparticles via surface exchange [30–32].

The loading of catalyst ferrous–ferric oxide nanoparticles is crucial since it considerably affects the dye degradation reaction. Increased catalyst addition can result in a more rapid decolorization of the organic component, such as dispersing 277 textile dye. However, until a specific saturation level is reached, the decolorization process is wholly slowed down or even halted. The degradation of dyes rises with increasing H_2O_2 concentration, as the concentration of H_2O_2 is proportional to the amount of OH^- radicals, which are critical in the oxidation process. The added concentration of H_2O_2 should be maximized for dye degradation efficiency. Excess H_2O_2 did not particularly or ultimately affect the deterioration [33].

In addition, the pH condition also significantly affects the degradation of dyes [34–36]. The scavenging effect decreases at a higher pH due to the slow generation of radical hydroxyl molecules. It resulted in the regeneration of Fe^{+2} and the synthesis of $Fe(OH)_2$, which was then oxidized to $Fe(OH)_3$ precipitates in the reaction. However, the ideal pH for ferrous–ferric oxide nanoparticles to increase degradation efficiency is essential. In the Fenton-like reaction, Fe^{+2} was oxidized to Fe^{+3} in the light to generate hydroxyl radicals to remove dyes. Numerous studies have demonstrated that the ideal pH range for dye removal is between 3 and 11 [37]. This study's optimum condition for dye removal was pH 7.0, which concurred with the published research. Oxalic acid is a better option to offer a reaction in a wider pH range with less production of iron sludge after the reaction.

It was demonstrated that a Disperse Red 277 was degraded in 180 min utilizing economically active ferrous–ferric oxide nanoparticles. The addition of H_2O_2 or oxalic acid was shown to enhance the degradation efficiency. Many studies have established that hydroxyl radicals are the primary source of Fenton reactions; these molecules were adsorbed on the surface of the nanoparticles [38,39]. Moreover, hydroxyl radicals adsorbed on the surface of ferrous–ferric oxide nanoparticles effectively enhanced dye degradation by acting as the primary oxidative species to attack Disperse Red 277 molecules. Another mediator, oxalic acid, was investigated because H_2O_2 is cytotoxic and causes cell death. A photo-Fenton-like reaction was established with ferrous–ferric oxide nanoparticles of oxalic acids. The ferrous–ferric oxide nanoparticles operated primarily as photocatalysts, while oxalic acids were stimulated to form electron–hole pairs [40,41]. It was shown that the ferrous–ferric-oxide-nanoparticle–oxalic-acid complexes might exhibit a strong potential for charge transformation from ligand to metal. The oxalic acids were initially adsorbed onto the surfaces of ferrous–ferric oxide nanoparticles, forming iron-oxide–oxalic-acid complexes with $[Fe^{III}(C_2O_4)_n]^{(2n-3)-}$ or $[Fe^{II}(C_2O_4)_{n-1}]^{4-2n}$ that were significantly more photoactive than other ferric species, generating the radical oxalate molecules, $C_2O_4^{\bullet-}$; then, a fast decarboxylation reaction occurred. The oxalate radicals were converted to the carbon-centered radical $CO_2^{\bullet-}$ and lastly to the superoxide anion radicals ($O_2^{\bullet-}$). Finally, $O_2^{\bullet-}$ disproportionately created hydrogen superoxide (H_2O_2) and O_2. The hydroxyl radicals ($^{\bullet}OH$) were produced during redox reactions by the consumption of H_2O_2 and were required for photodegradation [42].

The radical chain process may occur when ferric-oxalate complexes are photolyzed to generate H_2O_2 and Fe^{3+}. The photochemical reduction of the ferric complexes is coupled with the Fenton reaction and produces reactive oxygen species, such as $O_2^{\bullet-}$, H_2O_2, and $^{\bullet}OH$ [43]. This reaction can be accomplished by using natural materials, such as ferrous–ferric oxide nanoparticles and oxalic acids, to generate hydroxyl radicals to replace the use of H_2O_2 [44].

This study confirmed that the Disperse Red 277 dye was degraded after treatment, and LC-MS confirmed the color-removing property of ferrous–ferric oxide nanoparticles. This is the first report determining the ion chromatogram for $[M+H]^+$ at m/z 383.25 for Disperse Red 277. The iron oxide nanomaterials could be used as nanoadsorbents in dye-containing water treatment to increase dye removal efficiency. However, the effectiveness of metal-oxide nanoparticles depends on various parameters including types of metal nanoparticles, sources of light, types of dyes and the reaction time (Table 3). The contaminants could be transformed into lesser hazardous materials by the photocatalytic reactions. After 180 min, the Disperse Red 277 was almost entirely degraded and demineralized by ferrous–ferric oxide nanoparticles. Fortunately, most textile effluents contain acidic color molecules, making the Fenton or photo-Fenton method ideal for removing color and COD in acidic environments [45]. The oxalic acid-assisted photo-Fenton catalytic process effectively degraded the dye completely within 180 min. This demonstrates the successful overcoming of the limitations associated with the traditional Fenton process, namely its poor degradation efficiency due to sludge formation and restricted pH range [46].

In summary, photocatalysis is considered a state-of-the-art photochemical approach, and it has been incredibly effective in the photodegradation of organic contaminants in wastewater [47]. The ferrous–ferric oxide nanoparticles with magnetic properties have the potential to be excellent photocatalysts capable of absorbing visible light. In addition, with properties such as cost-effectiveness, high capacity of adsorption and stability, and ease of separation, ferrous–ferric oxide nanoparticles are ideal for industrial effluent treatment [48,49]. Moreover, ferrous–ferric oxide nanoparticles may exhibit exceptional excellence as nanoadsorbents and appear to be the most promising material for effective metal ion removal from wastewater [31]. However, to fully elucidate the thermodynamic and structural changes, as well as the stability of the nanoparticles as a catalyst, pre- and post-reaction analysis of the nanoparticles using XRD and TEM is crucial. This analysis is essential for optimizing the photodegradation process towards continuous operation and reusability for industrial viability.

Table 3. Photocatalytic dye degradation using different metal-oxide and metal-doped metal-oxide nanoparticles.

Sr. No.	Nanoparticles	Light Sources	Dye	Degradation Time (Min.)	Degradation (%)	References
1	ZnO	UV light	Methyl orange	180	89.6	[50]
2	ZnO	UV light	Methylene blue	200	69.0	[51]
3	$CeO_2/CoWO_4$	Visible light	Methylene blue	105	92.5	[52]
4	MgO	UV light	Methylene blue	120	75.0	[53]
5	ZnMgO	UV light	Methylene blue	60	87.0	[54]
6	CaO-MgO	UV light	Methylene blue	100	44.0	[55]
7	Co-CeO_2	Sunlight	Methylene blue	180	29.0	[56]
8	Ag_2S-MgO-GO	UV light	Rhodamine B	60	98.8	[57]
9	NiO and Fe-NiO	Visible light	Rhodamine B	40	73.0 and 99.0	[58]
10	Ag-Fe_2O_3	Visible light	Phenol red	8	78.0	[59]
11	Fe_2O_3	Xenon arc lamp	Methylene blue	120	63.6	[60]
12	Hematite (α-Fe_2O_3)	Sunlight	Bromophenol blue	240	87.9	[61]
13	MoO_3	Xenon lamp	Alizarin	120	74.0	[62]
14	TiO_2	Sunlight	Crystal violet	45	90.5	[63]
15	TiO_2	Mercury lamp	Sudan black B	100	96.0	[64]
16	SnO_2	Mercury lamp	Eriochrome black T	270	77.0	[65]
17	CuO	Sun light	Methyl red	135	85.0	[66]
18	ZrO_2	Sun light	Reactive yellow 160	120	94.0	[67]
19	NiO	Sun light	Congo red	160	84.0	[68]
20	Fe_3O_4	Visible Light	Disperse red 277	180	100	Present work

5. Conclusions

The catalytic efficacy of ferrous–ferric oxide nanoparticles is dose-dependent and influenced by H_2O_2, oxalic acid content, and pH. This photocatalyst is suitable for continuous decolorization and degradation processes, with optimal results achieved at a neutral pH and a nanoparticle concentration of 1.0 g/L. The nanoparticles can replace H_2O_2 with oxalic acid in a Fenton-like reaction, leading to visible light-dependent photocatalysis of textile dye. Complete removal of dye within 3 h suggests industrial applicability. Oxalic acid-mediated enhanced adsorption capabilities and the magnetic characteristics of ferrous–ferric oxide nanoparticles can help to complete the removal of Disperse Red 277 dye. These nanoparticles could lead to the development of new adsorption nanomaterials with high absorption capacity and efficient separation, offering more cost-effective environmental remediation options for industrial effluent treatment. The pseudo-first-order kinetics nature of the dye degradation offers predictable rates and easier control and facilitates continuous treatment systems. Nanoremediation using nanoparticles, offers a cost-effective and efficient solution for large-scale contamination cleanup, though careful assessment is crucial to prevent environmental harm. Improved understanding and utilization of nanoparticles in environmental applications show promise for future advancements.

Supplementary Materials: The following supporting information can be downloaded at: https://www.mdpi.com/article/10.3390/chemengineering8040067/s1, Table S1: Base reaction experiment to degrade 50 ppm dye using 60 mM H_2O_2; Table S2: Base reaction experiment to degrade 50 ppm dye using 60 mM oxalic acid.

Author Contributions: Conceptualization, S.B., P.D. and D.J.H.S.; methodology, S.B. and P.D.; software, S.B.; validation, S.B., P.D. and D.J.H.S.; formal analysis, S.B. and P.D.; investigation, S.B., P.D. and A.G.; resources, S.B., P.D., I.N.W. and D.J.H.S.; data curation, S.B., A.G., Q.-T.P. and Y.-Y.C.; writing—original draft preparation, S.B., P.D. and D.J.H.S.; writing—review and editing, P.D., Q.-T.P., Y.-Y.C. and D.J.H.S.; visualization, S.B.; supervision, P.D. and D.J.H.S. All authors have read and agreed to the published version of the manuscript.

Funding: The authors gratefully acknowledge the University Grant Commission (UGC), Govt. of India, New Delhi, that funded the work as part of SAP (Special Assistance Programme) and BSR support for this research under the grant 7/327/2011 awarded to Department of Biosciences, Veer Narmad South Gujarat University, Surat, Gujarat, India.

Data Availability Statement: Data is contained within the article or Supplementary Material.

Acknowledgments: We are grateful for the research facilities of DST-FIST-I and resources by the Department of Biosciences, Veer Narmad South Gujarat University, and the Department of Biological Science and Technology, National Pingtung University of Science and Technology for collaborative work.

Conflicts of Interest: The authors declare no conflicts of interest.

References

1. Khan, W.U.; Ahmed, S.; Dhoble, Y.; Madhav, S. A Critical Review of Hazardous Waste Generation from Textile Industries and Associated Ecological Impacts. *J. Indian Chem. Soc.* **2023**, *100*, 100829. [CrossRef]
2. Saratale, R.G.; Saratale, G.D.; Chang, J.-S.; Govindwar, S.P. Decolorization and Biodegradation of Textile Dye Navy Blue HER by Trichosporon Beigelii NCIM-3326. *J. Hazard. Mater.* **2009**, *166*, 1421–1428. [CrossRef]
3. El Harfi, S.; El Harfi, A. Classifications, Properties and Applications of Textile Dyes: A Review. *Appl. J. Environ. Eng. Sci.* **2017**, *3*, 311–320.
4. Kallawar, G.A.; Bhanvase, B.A. A Review on Existing and Emerging Approaches for Textile Wastewater Treatments: Challenges and Future Perspectives. *Environ. Sci. Pollut. Res.* **2024**, *31*, 1748–1789. [CrossRef]
5. Bhavsar, S.; Dudhagara, P.; Tank, S. R Software Package Based Statistical Optimization of Process Components to Simultaneously Enhance the Bacterial Growth, Laccase Production and Textile Dye Decolorization with Cytotoxicity Study. *PLoS ONE* **2018**, *13*, e0195795. [CrossRef]
6. Clark, M. *Handbook of Textile and Industrial Dyeing: Principles, Processes and Types of Dyes*; Elsevier: Amsterdam, The Netherlands, 2011; ISBN 0857093975.

7. Belessiotis, G.V.; Falara, P.P.; Ibrahim, I.; Kontos, A.G. Magnetic Metal Oxide-Based Photocatalysts with Integrated Silver for Water Treatment. *Materials* **2022**, *15*, 4629. [CrossRef]
8. Emran, M.Y.; Miran, W.; Gomaa, H.; Ibrahim, I.; Belessiotis, G.V.; Abdelwahab, A.A. *Handbook of Biodegradable Materials*; Springer: Berlin/Heidelberg, Germany, 2022; ISBN 9783030837839.
9. Kefeni, K.K.; Mamba, B.B. Photocatalytic Application of Spinel Ferrite Nanoparticles and Nanocomposites in Wastewater Treatment. *Sustain. Mater. Technol.* **2020**, *23*, e00140. [CrossRef]
10. Ohtani, B. Photocatalysis A to Z—What We Know and What We Do Not Know in a Scientific Sense. *J. Photochem. Photobiol. C Photochem. Rev.* **2010**, *11*, 157–178. [CrossRef]
11. Sanford, J.R.; Larson, R.A.; Runge, T. Nitrate Sorption to Biochar Following Chemical Oxidation. *Sci. Total Environ.* **2019**, *669*, 938–947. [CrossRef]
12. Shan, R.; Lu, L.; Gu, J.; Zhang, Y.; Yuan, H.; Chen, Y.; Luo, B. Photocatalytic Degradation of Methyl Orange by Ag/TiO_2/Biochar Composite Catalysts in Aqueous Solutions. *Mater. Sci. Semicond. Process.* **2020**, *114*, 105088. [CrossRef]
13. Nie, C.; Wang, J.; Cai, B.; Lai, B.; Wang, S.; Ao, Z. Multifunctional Roles of MoS_2 in Persulfate-Based Advanced Oxidation Processes for Eliminating Aqueous Organic Pollutants: A Review. *Appl. Catal. B Environ.* **2023**, *340*, 123173. [CrossRef]
14. Neon, M.H.K.; Islam, M.S. MoO_3 and Ag Co-Synthesized TiO_2 as a Novel Heterogeneous Photocatalyst with Enhanced Visible-Light-Driven Photocatalytic Activity for Methyl Orange Dye Degradation. *Environ. Nanotechnol. Monit. Manag.* **2019**, *12*, 100244.
15. Dudita, M.; Bogatu, C.; Enesca, A.; Duta, A. The Influence of the Additives Composition and Concentration on the Properties of SnOx Thin Films Used in Photocatalysis. *Mater. Lett.* **2011**, *65*, 2185–2189. [CrossRef]
16. Enesca, A.; Isac, L.; Duta, A. Charge Carriers Injection in Tandem Semiconductors for Dyes Mineralization. *Appl. Catal. B Environ.* **2015**, *162*, 352–363. [CrossRef]
17. He, S.; Li, W.; Wang, X.; Ma, Q.; Li, M.; Xu, W.; Wang, X.; Zhao, C. High-Efficient Precious-Metal-Free g-C_3N_4-Fe_3O_4/β-FeOOH Photocatalyst Based on Double-Heterojunction for Visible-Light-Driven Hydrogen Evolution. *Appl. Surf. Sci.* **2020**, *506*, 144948. [CrossRef]
18. Bekhit, F.; Farag, S.; Attia, A.M. Decolorization and Degradation of the Azo Dye by Bacterial Cells Coated with Magnetic Iron Oxide Nanoparticles. *Environ. Nanotechnol. Monit. Manag.* **2020**, *14*, 100376. [CrossRef]
19. Manohar, A.; Vijayakanth, V.; Vattikuti, S.V.P.; Kim, K.H. A Mini-Review on AFe_2O_4 (A = Zn, Mg, Mn, Co, Cu, and Ni) Nanoparticles: Photocatalytic, Magnetic Hyperthermia and Cytotoxicity Study. *Mater. Chem. Phys.* **2022**, *286*, 126117. [CrossRef]
20. Egea-Benavente, D.; Díaz-Ufano, C.; Gallo-Cordova, Á.; Palomares, F.J.; Cuya Huaman, J.L.; Barber, D.F.; Morales, M.d.P.; Balachandran, J. Cubic Mesocrystal Magnetic Iron Oxide Nanoparticle Formation by Oriented Aggregation of Cubes in Organic Media: A Rational Design to Enhance the Magnetic Hyperthermia Efficiency. *ACS Appl. Mater. Interfaces* **2023**, *15*, 32162–32176. [CrossRef]
21. Parida, K.M.; Naik, B. Synthesis of Mesoporous TiO_2-XNx Spheres by Template Free Homogeneous Co-Precipitation Method and Their Photo-Catalytic Activity under Visible Light Illumination. *J. Colloid Interface Sci.* **2009**, *333*, 269–276. [CrossRef]
22. Vaidyanathan, G.; Sendhilnathan, S. Characterization of $Co1-XZnxFe_2O_4$ Nanoparticles Synthesized by Co-Precipitation Method. *Phys. B Condens. Matter* **2008**, *403*, 2157–2167. [CrossRef]
23. Raja, M. Green Synthesis of Iron Nanoparticles and Investigation of Their Effect on Degradation of Dyes. *J. Biol. Inf. Sci.* **2015**, *4*, 6–8.
24. Villegas, V.A.R.; Ramírez, J.I.D.L.; Guevara, E.H.; Sicairos, S.P.; Ayala, L.A.H.; Sanchez, B.L. Synthesis and Characterization of Magnetite Nanoparticles for Photocatalysis of Nitrobenzene. *J. Saudi Chem. Soc.* **2020**, *24*, 223–235. [CrossRef]
25. Kim, W.; Suh, C.Y.; Cho, S.W.; Roh, K.M.; Kwon, H.; Song, K.; Shon, I.J. A New Method for the Identification and Quantification of Magnetite-Maghemite Mixture Using Conventional X-Ray Diffraction Technique. *Talanta* **2012**, *94*, 348–352. [CrossRef] [PubMed]
26. Zhang, S.; Wu, W.; Xiao, X.; Zhou, J.; Ren, F.; Jiang, C. Preparation and Characterization of Spindle-like Fe_3O_4 Mesoporous Nanoparticles. *Nanoscale Res. Lett.* **2011**, *6*, 89. [CrossRef]
27. Zhang, Z.; Wang, G.; Li, W.; Zhang, L.; Guo, B.; Ding, L.; Li, X. Photocatalytic Activity of Magnetic Nano-β-FeOOH/Fe_3O_4/Biochar Composites for the Enhanced Degradation of Methyl Orange under Visible Light. *Nanomaterials* **2021**, *11*, 526. [CrossRef]
28. Ambashta, R.D.; Sillanpää, M. Water Purification Using Magnetic Assistance: A Review. *J. Hazard. Mater.* **2010**, *180*, 38–49. [CrossRef] [PubMed]
29. Mahdavian, A.R.; Mirrahimi, M.A.-S. Efficient Separation of Heavy Metal Cations by Anchoring Polyacrylic Acid on Superparamagnetic Magnetite Nanoparticles through Surface Modification. *Chem. Eng. J.* **2010**, *159*, 264–271. [CrossRef]
30. Ma, Z.-Y.; Guan, Y.-P.; Liu, X.-Q.; Liu, H.-Z. Preparation and Characterization of Micron-Sized Non-Porous Magnetic Polymer Microspheres with Immobilized Metal Affinity Ligands by Modified Suspension Polymerization. *J. Appl. Polym. Sci.* **2005**, *96*, 2174–2180. [CrossRef]
31. Hu, H.; Wang, Z.; Pan, L. Synthesis of Monodisperse Fe_3O_4@silica Core–Shell Microspheres and Their Application for Removal of Heavy Metal Ions from Water. *J. Alloys Compd.* **2010**, *492*, 656–661. [CrossRef]
32. Zhao, X.; Wang, J.; Wu, F.; Wang, T.; Cai, Y.; Shi, Y.; Jiang, G. Removal of Fluoride from Aqueous Media by Fe_3O_4@$Al(OH)_3$ Magnetic Nanoparticles. *J. Hazard. Mater.* **2010**, *173*, 102–109. [CrossRef]
33. Movahedyan, H.; Mohammadi, A.S.; Assadi, A. Comparison of Different Advanced Oxidation Processes Degrading P-Chlorophenol in Aqueous Solution. *J. Environ. Health Sci. Eng.* **2009**, *6*, 153–160.

34. Kavitha, S.K.; Palanisamy, P.N. Photocatalytic and Sonophotocatalytic Degradation of Reactive Red 120 Using Dye Sensitized TiO_2 under Visible Light. *Int. J. Civ. Environ. Eng.* **2011**, *3*, 1–6.
35. Rauf, M.A.; Ashraf, S.S. Fundamental Principles and Application of Heterogeneous Photocatalytic Degradation of Dyes in Solution. *Chem. Eng. J.* **2009**, *151*, 10–18. [CrossRef]
36. Sabhi, S.; Kiwi, J. Degradation of 2, 4-Dichlorophenol by Immobilized Iron Catalysts. *Water Res.* **2001**, *35*, 1994–2002. [CrossRef] [PubMed]
37. Dindarloo Inaloo, K.; Naddafi, K.; Mesdaghinia, A.R.; Nasseri, S.; Nabizadeh Nodehi, R.; Rahimi, A. Optimization of operational parameters for decolorization and degradation of ci reactive blue 29 by ozone. *Iran. J. Environ. Health Sci. Eng.* **2011**, *8*, 227–234.
38. Fernandez, J.; Dhananjeyan, M.R.; Kiwi, J.; Senuma, Y.; Hilborn, J. Evidence for Fenton Photoassisted Processes Mediated by Encapsulated Fe Ions at Biocompatible PH Values. *J. Phys. Chem. B* **2000**, *104*, 5298–5301. [CrossRef]
39. Lim, H.; Lee, J.; Jin, S.; Kim, J.; Yoon, J.; Hyeon, T. Highly Active Heterogeneous Fenton Catalyst Using Iron Oxide Nanoparticles Immobilized in Alumina Coated Mesoporous Silica. *Chem. Commun.* **2006**, 463–465. [CrossRef] [PubMed]
40. Leland, J.K.; Bard, A.J. Photochemlstry of Colloidal Semiconducting Iron Oxlde Polymorphs. *J. Phys. Chem.* **1987**, *91*, 5076–5083. [CrossRef]
41. Siffert, C.; Sulzberger, B. Light-Induced Dissolution of Hematite in the Presence of Oxalate. A Case Study. *Langmuir* **1991**, *7*, 1627–1634. [CrossRef]
42. Xu, P.; Zeng, G.M.; Huang, D.L.; Feng, C.L.; Hu, S.; Zhao, M.H.; Lai, C.; Wei, Z.; Huang, C.; Xie, G.X.; et al. Use of Iron Oxide Nanomaterials in Wastewater Treatment: A Review. *Sci. Total Environ.* **2012**, *424*, 1–10. [CrossRef]
43. Quici, N.; Morgada, M.E.; Piperata, G.; Babay, P.; Gettar, R.T.; Litter, M.I. Oxalic Acid Destruction at High Concentrations by Combined Heterogeneous Photocatalysis and Photo-Fenton Processes. *Catal. Today* **2005**, *101*, 253–260. [CrossRef]
44. Faust, B.C.; Zepp, R.G. Photochemistry of Aqueous Iron (III)-Polycarboxylate Complexes: Roles in the Chemistry of Atmospheric and Surface Waters. *Environ. Sci. Technol.* **1993**, *27*, 2517–2522. [CrossRef]
45. Christian, D.; Gaekwad, A.; Dani, H.; Shabiimam, M.A.; Kandya, A. Recent Techniques of Textile Industrial Wastewater Treatment: A Review. *Mater. Today Proc.* **2023**, *77*, 277–285. [CrossRef]
46. Xiao, C.; Li, S.; Yi, F.; Zhang, B.; Chen, D.; Zhang, Y.; Chen, H.; Huang, Y. Enhancement of photo-Fenton catalytic activity with the assistance of oxalic acid on the kaolin–FeOOH system for the degradation of organic dyes. *RSC Adv.* **2020**, *10*, 18704–18714. [CrossRef]
47. Akhavan, O.; Azimirad, R. Photocatalytic Property of Fe_2O_3 Nanograin Chains Coated by TiO_2 Nanolayer in Visible Light Irradiation. *Appl. Catal. A Gen.* **2009**, *369*, 77–82. [CrossRef]
48. Fan, F.-L.; Qin, Z.; Bai, J.; Rong, W.-D.; Fan, F.-Y.; Tian, W.; Wu, X.-L.; Wang, Y.; Zhao, L. Rapid Removal of Uranium from Aqueous Solutions Using Magnetic Fe_3O_4@SiO_2 Composite Particles. *J. Environ. Radioact.* **2012**, *106*, 40–46. [CrossRef]
49. Hu, J.; Chen, G.; Lo, I.M.C. Removal and Recovery of Cr(VI) from Wastewater by Maghemite Nanoparticles. *Water Res.* **2005**, *39*, 4528–4536. [CrossRef]
50. Asif, M.; Shafiq, M.; Imtiaz, F.; Ahmed, S.; Alazba, A.A.; Hussain, H.N.; Butt, F.N.; Zainab, S.A.; Khan, M.K.; Bilal, M. Photocatalytic Degradation of Methyl Orange from Aqueous Solution Using ZnO by Response Surface Methodology. *Top Catal.* **2024**, *67*, 1–9. [CrossRef]
51. Kahsay, M.H. Synthesis and characterization of ZnO nanoparticles using aqueous extract of Becium grandiflorum for antimicrobial activity and adsorption of methylene blue. *Appl. Water Sci.* **2021**, *11*, 45. [CrossRef]
52. Selvi, S.; Rajendran, R.; Barathi, D.; Jayamani, N. Facile Synthesis of CeO_2/$CoWO_4$ Hybrid Nanocomposites for High Photocatalytic Performance and Investigation of Antimicrobial Activity. *J. Electron. Mater.* **2021**, *50*, 2890–2902. [CrossRef]
53. Balakrishnan, G.; Velavan, R.; Batoo, K.M.; Raslan, E.H. Microstructure, optical and photocatalytic properties of MgO nanoparticles. *Results Phys.* **2020**, *16*, 103013. [CrossRef]
54. Sierra-Fernandez, A.; De la Rosa-García, S.C.; Gomez-Villalba, L.S.; Gómez-Cornelio, S.; Rabanal, M.E.; Fort, R.; Quintana, P. Synthesis, Photocatalytic, and Antifungal Properties of MgO, ZnO and Zn/Mg Oxide Nanoparticles for the Protection of Calcareous Stone Heritage. *ACS Appl. Mater. Interfaces* **2017**, *9*, 24873–24886. [CrossRef]
55. Shahid, M.; Farrukh, M.A.; Umar, A.A.; Khaleeq-ur-Rahman, M. Solvent controlled synthesis of CaO-MgO nanocomposites and their application in the photodegradation of organic pollutants of industrial waste. *Russ. J. Phys. Chem. A* **2014**, *88*, 836–844. [CrossRef]
56. George, S.E.; George, M.; Alex, J.; Joy, L.K.; Aravind, A.; Sajan, D.; Thakur, A.; Hussain, S.; Vinitha, G. Nonlinear optical and photocatalytic dye degradation of Co doped CeO_2 nanostructures synthesized through a modified combustion technique. *Ceram. Int.* **2020**, *46*, 13932–13940. [CrossRef]
57. Wang, H.; Li, G.; Fakhri, A. Fabrication and structural of the Ag_2S-MgO/graphene oxide nanocomposites with high photocatalysis and antimicrobial activities. *J. Photochem. Photobiol. B Biol.* **2020**, *207*, 111882. [CrossRef]
58. Minisha, S.; Johnson, J.; Mohammad Wabaidur, S.; Gupta, J.K.; Aftab, S.; Siddiqui, M.R.; Lai, W.C. Synthesis and characterizations of Fe-doped NiO nanoparticles and their potential photocatalytic dye degradation activities. *Sustainability* **2023**, *15*, 14552. [CrossRef]
59. Idris, D.S.; Roy, A. Antioxidant and dye degradation activity of green synthesized silver-iron oxide (Ag-Fe_2O_3) bimetallic nanoparticles. *Nano-Struct. Nano-Objects* **2024**, *38*, 101142. [CrossRef]

60. Subaihi, A.; Naglah, A.M. Facile synthesis and characterization of Fe_2O_3 nanoparticles using L-lysine and L-serine for efficient photocatalytic degradation of methylene blue dye. *Arab. J. Chem.* **2022**, *15*, 103613. [CrossRef]
61. Ahmed, A.; Usman, M.; Yu, B.; Shen, Y.; Cong, H. Sustainable fabrication of hematite (α-Fe_2O_3) nanoparticles using biomolecules of Punica granatum seed extract for unconventional solar-light-driven photocatalytic remediation of organic dyes. *J. Mol. Liq.* **2021**, *339*, 116729. [CrossRef]
62. Bharathi, D.; AlSalhi, M.S.; Devanesan, S.; Nandagopal, J.G.T.; Kim, W.; Ranjithkumar, R. Photocatalytic degradation of Rhodamine B using green-synthesized ZnO nanoparticles from Sechium edule polysaccharides. *Appl. Nanosci.* **2022**, *12*, 2477–2487. [CrossRef]
63. Balaraman, P.; Balasubramanian, B.; Liu, W.C.; Kaliannan, D.; Durai, M.; Kamyab, H.; Alwetaishi, M.; Maluventhen, V.; Ashokkumar, V.; Chelliapan, S.; et al. Sargassum myriocystum-mediated TiO_2-nanoparticles and their antimicrobial, larvicidal activities and enhanced photocatalytic degradation of various dyes. *Environ. Res.* **2022**, *204*, 112278. [CrossRef]
64. Safaralizadeh, E.; Darzi, S.J.; Mahjoub, A.R.; Abazari, R. Visible light-induced degradation of phenolic compounds by Sudan black dye sensitized TiO_2 nanoparticles as an advanced photocatalytic material. *Res. Chem. Intermediat.* **2017**, *43*, 1197–1209. [CrossRef]
65. Najjar, M.; Hosseini, H.A.; Masoudi, A.; Sabouri, Z.; Mostafapour, A.; Khatami, M.; Darroudi, M. Green chemical approach for the synthesis of SnO_2 nanoparticles and its application in photocatalytic degradation of Eriochrome Black T dye. *Optik* **2021**, *242*, 167152. [CrossRef]
66. Dulta, K.; Koşarsoy Ağçeli, G.; Chauhan, P.; Jasrotia, R.; Chauhan, P.K.; Ighalo, J.O. Multifunctional CuO nanoparticles with enhanced photocatalytic dye degradation and antibacterial activity. *Sustain. Environ. Res.* **2022**, *32*, 2. [CrossRef]
67. Al-Zaqri, N.; Muthuvel, A.; Jothibas, M.; Alsalme, A.; Alharthi, F.A.; Mohana, V. Biosynthesis of zirconium oxide nanoparticles using Wrightia tinctoria leaf extract: Characterization, photocatalytic degradation and antibacterial activities. *Inorg. Chem. Commun.* **2021**, *127*, 108507. [CrossRef]
68. Bhat, S.A.; Zafar, F.; Mondal, A.H.; Kareem, A.; Mirza, A.U.; Khan, S.; Mohammad, A.; Haq, Q.M.R.; Nishat, N. Photocatalytic degradation of carcinogenic Congo red dye in aqueous solution, antioxidant activity and bactericidal effect of NiO nanoparticles. *J. Iran. Chem. Soc.* **2020**, *17*, 215–227. [CrossRef]